PCCP

Accepted Manuscript

This is an *Accepted Manuscript*, which has been through the Royal Society of Chemistry peer review process and has been accepted for publication.

Accepted Manuscripts are published online shortly after acceptance, before technical editing, formatting and proof reading. Using this free service, authors can make their results available to the community, in citable form, before we publish the edited article. We will replace this *Accepted Manuscript* with the edited and formatted *Advance Article* as soon as it is available.

You can find more information about *Accepted Manuscripts* in the **Information for Authors**.

Please note that technical editing may introduce minor changes to the text and/or graphics, which may alter content. The journal's standard **Terms & Conditions** and the **Ethical guidelines** still apply. In no event shall the Royal Society of Chemistry be held responsible for any errors or omissions in this *Accepted Manuscript* or any consequences arising from the use of any information it contains.

Journal Name

ARTICLE TYPE

Soft X-ray absorption spectroscopy of Ar$_2$ and ArNe dimers and small Ar clusters.[†]

Ghazal Jabbari,[a] Tsveta Miteva,[a] Vasili Stumpf,[a] Kirill Gokhberg,[a] Patrick O'Keeffe,[b] Alessandra Ciavardini,[b] Paola Bolognesi,[b] Marcello Coreno,[b] Lorenzo Avaldi,[b] Elham Keshavarz,[c] Maryam Ghandehari,[d] Manijeh Tozihi,[e] Carlo Callegari,[f] Michele Alagia,[h] Kevin Charles Prince,[f,g,h] Antti Kivimäki,[h] and Robert Richter[f]

The X-ray absorption spectra (XAS) of Ar$_2$ and ArNe dimers and small Ar clusters in the L$_{2,3}$ region (244-252 eV) of the Ar atom have been recorded using synchrotron light and a combination of coincidence methods and kinetic energy discrimination of energetic ions. The absorption peaks in the spectra of the dimers and clusters were found to be shifted and broadened relative to the peaks in the spectrum of the Ar atom. In order to unambiguously relate these chemical shifts to the electronic structure of the core excited states in dimers, we performed *ab initio* calculations of the XAS spectra. Implications of the results for the use of XAS as a structure determination method in large rare gas clusters are discussed.

1 Introduction

Core-hole spectroscopy is a widely used technique for the investigation of the geometric and electronic structure of gas-phase molecules, free clusters, surface adsorbates, and solids[1–4]. Counterintuitively, this is largely due to the fact that core-hole electrons, being more tightly bound, are more localized as compared to the valence electrons. The result is that the small changes in the binding energy of such electrons, called the chemical shift, can be more easily related to the chemical environment of the probed atom than those of the valence electrons which are de-

localized over several atoms. To obtain this simplification of the spectrum requires excitation or emission of core electrons which involves relatively high-energy photons and, furthermore, to be able to record spectra in the near-edge region of different atoms requires that the high-energy radiation be tunable in energy. With the advent of third generation synchrotron sources the difficulties mentioned above were overcome due to the ability of these sources to provide tunable soft X-ray radiation and, as a result, the core-hole spectroscopy technique has become widely available.

There are several varieties of core-hole spectroscopy such as X-ray photoelectron spectroscopy (XPS), Auger electron spectroscopy (AES), Resonant Auger electron spectroscopy (RAS) and X-ray absorption spectroscopy (XAS). In this paper we will concentrate on the XAS of rare gas dimers and small clusters in the L$_{2,3}$ region of Ar (245-252 eV). There is an extensive literature on the study of free clusters with synchrotron (for a recent review see [3]). Indeed, many of the pioneering studies of this field have involved the core-hole spectroscopy of Ar-containing rare gas clusters. The reason for the use of XAS in the study of clusters is that the shifts of the core-hole states have been shown to be easily related to the position of the atoms within the cluster and thus can be used for structure determination of the clusters. The first XAS studies[5,6] of Ar clusters involved scanning the synchrotron radiation in the L$_{2,3}$ region while recording electron and

[a] Theoretische Chemie, Physikalisch-Chemisches Institut, Universität Heidelberg, Im Neuenheimer Feld 229, 69120 Heidelberg, Germany

[b] CNR-ISM, Area della Ricerca di Roma 1, Monterotondo Scalo, Italy.

[c] Department of Chemistry, Isfahan University, Iran.

[d] Department of Chemistry, Isfahan University of Technology, Iran.

[e] Department of Chemistry, University of Zanjan, Zanjan 45371-38791, Iran.

[f] Elettra-Sincrotrone Trieste, Basovizza 34149, Italy.

[g] Molecular Model Discovery Laboratory, Department of Chemistry and Biotechnology, Faculty of Sciences, Engineering and Technology, Swinburne University of Technology, Melbourne, Victoria 3122, Australia.

[h] CNR-IOM, Area Science Park, 34149 Trieste, Italy.

† Electronic Supplementary Information (ESI) available: [Radial densities of the 4s and 5s orbitals of Ar and the transition moments between the ground state and core excited states of the Ar$_2$ amd ArNe]. See DOI: 10.1039/b000000x/

ion yields and varying the cluster size from few up to 750 Ar atoms. These studies revealed a shift of the $Ar(2p_{3/2}^{-1}4s)$ transition by ~ 1 eV in comparison to the atomic transition although at a resolution insufficient to fully resolve the contribution of bulk and surface atoms. Subsequent studies[7], with improved resolution and a wider range of cluster sizes, did resolve the contribution of the surface (shift of 0.7 eV) and bulk (shift of 1.0 eV) atoms for the $Ar(2p_{3/2}^{-1}4s)$ transition although the region of the higher lying resonances ($Ar(2p_{1/2}^{-1}4s)$ and $Ar(2p_{3/2}^{-1}3d)$) was too congested to yield useful information. Many of the concepts for describing the chemical shifts introduced in the latter paper were later developed into theories that describe the XPS and XAS of rare gas clusters[8]. Subsequent experimental work provided further detailed measurements of the XAS spectrum in the $L_{2,3}$ region both in pure Ar clusters[9,10] and in heterogeneous clusters containing mixtures such as Ar/Kr, Ar/Xe and Ar/N$_2$. [11,12]

Theories used to describe the shifts of core-excitation transition of atoms embedded in rare gas clusters or at surfaces[8,13–15] are often based on the modelling of the interaction of the Rydberg electron with the ion core (e-Rg$_{core}^{+}$) and that of the interaction of the Rydberg electron with the surrounding lattice (e-Rg$_{crystal}$). The potentials used to describe these interactions are based on model potentials where, for example, the e-Rg$_{core}^{+}$ potential can be described by the Kleinman-Bylander pseudopotential[8,16] and the e-Rg$_{crystal}$ is described by a model potential based on the sum of short and long range forces with the parameters adjusted to describe the low energy electron-Rg scattering (see [15]). Clearly these potentials should be able to describe the core-excited dimers investigated in this paper. We expect that the high-level *ab initio* calculations of the core-excited states in rare gas dimers which are quantitatively corroborated by experimental measurement presented here will provide the opportunity to rigorously test these model potentials. Furthermore, the measurement of the Ar$_2$ and ArNe XAS presented in the present paper involves much smaller changes (20 - 40 meV) in the XAS spectra with respect to the atom in comparison to large clusters (0.7-1.0 eV) which gives access to a previously unexplored regime for testing theoretical models. It should be noted that the above models are equally applicable (of course with a different electron-core potential) to the case where the Rydberg electron is that of an alkali-metal atom (A). There is a vast body of literature calculating in this fashion the potential energy curves of A-Rg van der Waals dimers[17,18], and the absorption spectra of A in Rg matrices[19,20]. The analogy between the two problems can be made more close by noting that the shell structure and charge state of the closed shell A$^+$ core are the same as in the core-excited Rg$^+$, and the equivalent-core (Z+1) approximation applies, of course with its limitations[21,22]. We will return to this point when qualitatively classifying our calculated Ar$_2$ and ArNe potential energy curves.

Another motivation for studying the XAS spectrum of rare gas

dimers and clusters is the recent proposal based on theoretical considerations[23–25] and subsequently demonstrated experimentally [26–28] of the possibility to control Interatomic Coulombic Decay (ICD) via the resonant Auger (RA) process. The general idea of this technique is that the kinetic energy (KE) of the ICD electrons can be controlled by steering the population of the states undergoing the ICD process using the RA process. By choosing different resonant excitations it is possible to change the relative populations of the excited states populated by the RA process. The utility of this scheme can be understood from the fact that the resonant process indirectly produces low energy electrons *via* ICD at the site of the targeted atom. The implications of the use of such a scheme for radiation damage on biological tissue is discussed in detail in[23]. The test experiments for demonstrating the control of the ICD process *via* the RA have been performed mostly on the rare gas dimers[26,27] largely due to the experimental ease in characterising the ICD process and the detailed knowledge of the RA process in the atoms. However, to fully exploit such a scheme it is necessary to understand the XAS of the relevant dimer/cluster in order to be able to choose well the energy of the exciting photon for the first step of the RA induced ICD.

To achieve the above aims we have performed a joint experimental and theoretical study of the core-hole spectroscopy of argon containing rare gas dimers and small clusters. The article is structured in the following manner: the computational details of the calculation of the potential energy curves (PECs) and Franck-Condon calculations used to simulate the core-hole spectra of the dimers are described in the next section. Then the experimental set-ups used to record the XAS core-hole spectra are outlined. In the results and discussion section we describe the experimental spectra of Ar, Ar$_2$ and ArNe recorded using the coincidence method as well as those of Ar$_2$ and small clusters of Ar recorded using a simplified experimental method. Subsequently, the calculated and experimental spectra are compared and all shifts and comparisons are discussed in detail.

2 Computational Details

Accurate *ab initio* ground state potential energy curves of Ar$_2$ and ArNe were taken from Ref.[29]. The equilibrium interatomic distances (binding energies) are 3.80 Å (12.0 meV) and 3.52 Å (5.6 meV) for Ar$_2$ and ArNe respectively.

Non-relativistic excitation energies at the Ar $L_{2,3}$-edge and the corresponding dipole transition moments as a function of the interatomic distance, R, were computed using the Algebraic Diagrammatic Construction (ADC) method for the polarization propagator[30,31]. In particular, we employed the ADC(2) extended scheme which uses a correlated ground state, correct up to second order in perturbation theory, and represents excited states expanded in the one-hole-one-particle (1h1p) and two-hole-two-particle (2h2p) configurations. The energies of singly excited

states and the corresponding transition moments in this scheme are correct respectively up to second and first order in perturbation theory.

The core-excited states of interest lie energetically high in the electronic continuum which is represented as a discretized pseudo-continuum in the *ab initio* calculations. While constructing the PECs, to avoid complications due to interactions between this pseudo-continuum and the core- excited resonances, we projected out the continuum states. Thus, the Hamiltonian was projected on the subspace Q given as, Q= $\{c_a^\dagger c_h |\Psi_0\rangle, c_a^\dagger c_b^\dagger c_i c_h |\Psi_0\rangle\}$. Here, the index h denotes the 2s and 2p orbitals of Ar in ArNe or their even and odd linear combinations of Ar in Ar_2, i denotes any valence orbital, while a and b stand for any virtual orbital; $|\Psi_0\rangle$ is the correlated ground state. The subspace Q comprises configurations necessary to describe both inter- and intra-atomic electron relaxation - the principal effect defining the energies of core-excited states[32]. Therefore, we expect no considerable loss of accuracy due to the projection operation. The projected ADC Hamiltonian, QHQ, is diagonalised for different R to produce the excitation energies and transition moments. Adding the ground state PEC to the excitation energies we obtained the core-excited PECs of interest. The core-ionized states were obtained using the ADC(2) extended method for the Green's function[?] , the aug-cc-pCVTZ basis set on Ar[33], and the same basis set on Ne as in the previous calculation. Similar to the core-excitation case, the Hamiltonian was projected on the subspace Q', where Q'= $\{c_h |\Psi_0\rangle, c_a^\dagger c_i c_h |\Psi_0\rangle\}$

The molecular orbitals and electron repulsive integrals needed for the ADC computations were obtained using the restricted Hartree-Fock procedure as implemented in the MOLCAS 7.4 package[34]. The calculations were carried out using the cc-pCVTZ basis set[33] on Ar augmented by 4 s-type, 4 p-type, and 4 d-type KBJ Rydberg-like orbitals[35]; the aug-cc-pVQZ basis set[36] was used on Ne. The vibrational states supported by the bound electronic PECs were calculated by diagonalizing the respective nuclear Hamiltonians represented on a uniformly spaced grid using a sine DVR basis[37]. The calculated energies of the v=0 states in the electronic ground states of the dimers are -10 meV in the case of Ar_2 and -4 meV in the case of ArNe.

For the computation of the theoretical X-ray absorption spectra it was assumed that both Ar_2 and ArNe are initially in the v=0 state of their respective ground electronic states. The spectra arising from the transitions to the bound core-excited states were constructed considering state- to-state transitions from the v=0 state of the ground electronic state to each vibrational level of the excited state. The intensities of each state-to-state transition were taken to be the generalised Franck-Condon factors computed using the corresponding vibrational wave functions and the ADC electronic transition moments.

In the case of the repulsive core-excited states, correlating with

$Ar(2p^{-1}4s)Ar$ and $Ar(2p^{-1}4s)Ne$ at asymptotic distances, the energy of the transition was taken as the difference between the v=0 level of the respective ground electronic state and the excited-state PEC at the equilibrium distance of each rare-gas dimer. The intensities of the lines were obtained by averaging the corresponding electronic transition moments over the v=0 wavefunction. This approximation is justified because the excited states PECs are flat and the electronic transition moments do not vary much in the Franck-Condon region. The spectra of the states correlating with $Ar(2p^{-1}3d\ ^1P)Ar$ and $Ar(2p^{-1}3d\ ^1P)Ne$ were obtained analogously.

Finally, the spectral peaks were generated by convolving the discrete transition lines with Lorentzian functions of FWHM 0.112 eV thus accounting for the lifetime broadening due to the Auger decay of the excited states[38]. For comparison with the experimental data the resulting spectrum is further convolved with a Gaussian of width 0.040 eV in order to account for the synchrotron photon resolution used in recording the XAS spectrum.

3 Experimental Set-ups

Two experimental apparatuses have been used to obtain the results presented in this work. Schematic illustrations of the two instruments and data acquisition chains are shown in Figures 1(a) and (b).

In both cases the interaction region was formed by the interaction, at right angles, of the focussed synchrotron radiation from the branch line of the Gas Phase beamline[39] of the Italian synchrotron source Elettra and a skimmed supersonic beam formed by expansion of rare gases through a 50 μm hole. Furthermore, in both experiments the synchrotron radiation was linearly polarized with its electric field vector parallel to the principal axis of the time of flight spectrometers. The synchrotron light can be continuously tuned from 13 to 280 eV. The supersonic beam was either formed from a static mixture of Ar and Ne (or Ar alone) or by using a double inlet system, in which the mixture could be optimized for dimer formation depending on the setup used. In the conditions used the dimers formed < 1 % of the beam while significant quantities of trimers and larger clusters were not detected.

The first set-up (see Figure 1(a)) consisted of a traditional PhotoElectron PhotoIon PhotoIon COincidence (PEPIPICO) spectrometer in which electrons were accelerated towards a microchannel plate detector at a distance of 17 mm from the interaction region while the ions were ejected in the opposite direction into a 10.5 cm Wiley McLaren ion time-of-flight spectrometer[40]. The signals from the electron detector were pre-amplified, discriminated and sent to the start channel of a time-to-digital converter (TDC) while the output of the ion detector was similarly treated and fed to the stop channel of the TDC (up to 32 stops can be recorded for each start). Electron-ion-ion maps were built
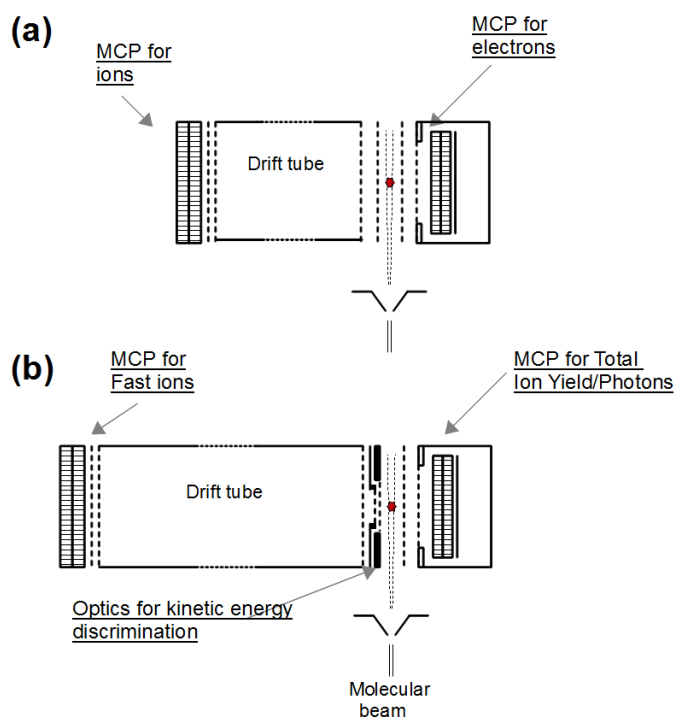
(a)

Fig. 1: Schematics of the two experimental apparatus employed to record the XAS spectra together with the synchrotron radiation from the Gas Phase beam line at Elettra. In panel (a) the coincidence set-up is shown in which the electrons are detected in coincidence with the ions detected on the opposite side of the apparatus. Panel (b) shows the modified apparatus which is used to detect the total ion yield on one side of the apparatus and only "fast" ions on the opposite side of the apparatus.

Fig. 2: Ion-ion map of the electron-ion-ion coincidences recorded in the region of the Ar $2p_{3/2}^{-1}5s$/Ar $2p_{3/2}^{-1}3d$ resonance using the experimental apparatus shown in Figure 1(a). Each event is represented by a dot on the map where the y-coordinate represents the arrival time of ion 2 and the x-coordinate is the arrival time of ion 1. The region shown contains the coincidences between the $^{20}Ne^+/Ar^+$, between $^{22}Ne^+/Ar^+$ and between Ar^+/Ar^+ which are seen as dark lines (multiple events) of slope -1. The vertical and horizontal lines show false coincidences.

up by selecting the events in which two ions were detected after a single start and in this map a 2D histogram of the flight time of the second ion was plotted against that of the first ion. An example of such an ion-ion map is shown in Figure 2(a) for this experimental setup for the case of an Ar/Ne expansion summed over a selection of photon energies corresponding to the excitation of the Ar $2p_{3/2}^{-1}3d$ resonance. The ion-ion coincidences resulting from the Coulomb explosion show up as a short line with slope of -1 centered on the point where ions with zero kinetic energy arrive. This is simply due to the fact that as a result of the Coulomb explosion ions with the same charge gain equal and opposite momentum with ions being ejected toward the detector arriving before ions with no initial KE component along the TOF axis while those which are emitted away from the detector arrive after. In the case of Ar^{2+}/Ar^+ coincidences the energy sharing changes and the slope of this line becomes -2 and therefore we can distinguish between these coincidences and Ne^+/Ar^+ coincidences. Finally, the horizontal and vertical lines are due to false coincidences in which one of the detected signals in coincidence with a real ion is completely uncorrelated with the other signal.
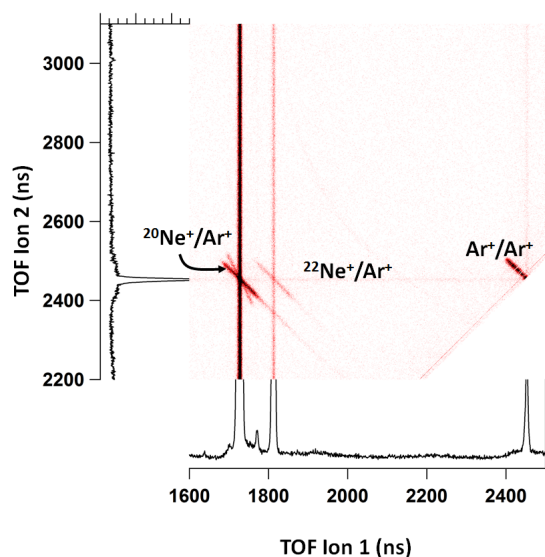
The experiment was performed by setting the photon energy and recording an ion-ion coincidence map then changing the photon energy and recording another map and so on. Each ion map was then analysed to extract the number of Ar^+/Ar^+ and Ar^+/Ne^+ coincidences corrected for false coincidences and then each of these were plotted as a function of photon energy; the analysis method is described in full in [40]. In typical conditions ~ 10 minutes per photon energy were required in order to achieve acceptable statistics resulting in a total acquisition time of over 43 hours for the spectrum shown in Figure 3.

In the second set-up the apparatus was modified to allow a better control of the electrostatic potentials in the various sections of the instrument. In this set-up both detectors were wired to detect ions. In particular on the drift tube side the acceleration section was shortened, and split into two parts with the help of an additional mesh (thus dividing the acceleration zone into two sections of lengths ~ 2 mm and ~ 5 mm respectively) while the flight tube was lengthened (to ~ 203 mm). By appropriate bias voltages applied to the meshes slow ions can be prevented from entering the drift tube. For the data shown this cut-off was set to 0.75 eV, allowing the exclusive detection of fragments produced by dissociation. The same potentials accelerate slow ions towards the MCP detector placed on the opposite side. Therefore ions produced by the ionization of atomic argon (the main component of the supersonic beam) dominate over the weak dimer signals.

As this detector is placed closer to the interaction region than the drift tube MCP a larger fraction of the emitted fluorescence UV (and soft x-ray) photons impinge on this detector. Nonetheless, the contribution of ions to the signal on both detectors is expected to be by far the dominant one.
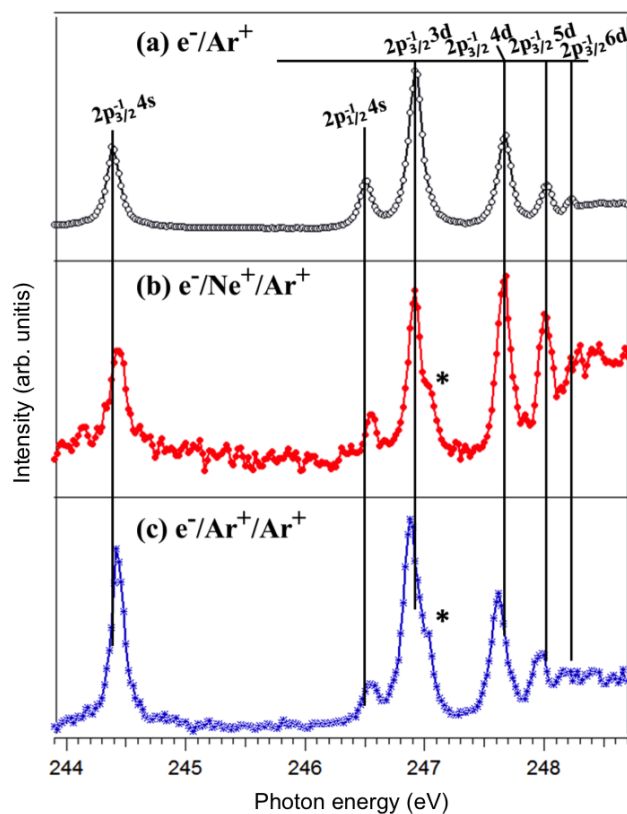

Fig. 3: Spectrum in the region of the Ar $2p_{3/2}^{-1}4s$, Ar $2p_{1/2}^{-1}4s$, Ar $2p_{3/2}^{-1}3d$, Ar $2p_{3/2}^{-1}4d$, and Ar $2p_{3/2}^{-1}5d$ resonances of the yield of (a) e^-/Ar^+, (b) $e^-/Ar^+/Ar^+$, and (c) $e^-/Ar^+/Ne^+$ coincidences as a function of the photon energy recorded using the experimental set-up shown in Figure 1 (a).

4 Results and Discussion

The dependence of the e^-/Ar^+, $e^-/Ar^+/Ar^+$ and $e^-/Ar^+/Ne^+$ coincidence yields on the photon energy is shown in Figure 3. In this range one observes the Ar $2p_{3/2}^{-1}4s$, Ar $2p_{3/2}^{-1}5s$ (overlapping with the 3d resonance), Ar $2p_{3/2}^{-1}3d$, Ar $2p_{3/2}^{-1}4d$ and Ar $2p_{3/2}^{-1}5d$ as well as the Ar $2p_{1/2}^{-1}4s$ resonances of the argon atom. It should be noted that although the Ar $2p_{3/2}^{-1}5s$ state has never been experimentally resolved from the transition to the Ar $2p_{3/2}^{-1}3d$ state we include it in our discussion as the *ab initio* calculations predict a significant contribution of this state to the soft X-ray absorption spectrum as described in detail below. In Figure 3 (a) the spectrum due to e^-/Ar^+ coincidences reflects simply the absorption

cross section of the argon atom in this range (see [38]). However, as described above, the co-expansion of argon and neon in the gas beam combined with the coincidence technique means that it is possible to record the XAS spectra of the Ar atom and ArNe and Ar_2 dimers simultaneously. It is therefore possible to reveal very small energy shifts of the peaks in the dimer spectra by the use of the atomic spectrum as an internal reference.

A careful comparison of the dimer spectra shown in Figure 3 (b) and (c) with the equivalent spectrum in the atom (Figure 3 (a)) reveals a number of observations which require explanation. For example, it is possible to see that the $2p_{3/2}^{-1}4s$ and Ar $2p_{1/2}^{-1}4s$ peaks in both the ArNe and Ar_2 dimer spectra are shifted to higher energy (by 40-60 meV depending on the peak and dimer) with respect to the corresponding peaks in the atomic spectrum. In contrast, while the $2p_{3/2}^{-1}3d$, $2p_{3/2}^{-1}4d$ and $2p_{3/2}^{-1}5d$ peaks in the ArNe spectrum exhibit negligible shifts, the equivalent peaks in the Ar_2 spectrum show clear negative energy shifts (approx. 50 meV) in comparison to the atomic spectrum. Furthermore there is a shoulder on the high energy side of the $2p_{3/2}^{-1}5s/2p_{3/2}^{-1}3d$ peaks in both the ArNe and Ar_2 spectra (highlighted by asterisks in Figures 3 (b) and (c)) and a change of the relative intensities of the $2p_{3/2}^{-1}$ nl peaks and the threshold region intensity of the ArNe case in comparison to the atomic and Ar_2 spectra. Each of these observations will be discussed in close comparison with theory below.

We first discuss the results of the second experiment shown in Figure 4. These results confirm the above observations for the Ar_2 dimer while extending the observed spectral region up to and above the $2p_{1/2}^{-1}$ threshold, containing the $2p_{1/2}^{-1}3d$, $2p_{1/2}^{-1}4d$ and $2p_{1/2}^{-1}5d$ resonances, in addition to those discussed above (see Figure 4 (a)). Furthermore, changing the expansion conditions of the supersonic jet allowed small clusters to be generated and the resulting spectrum to be recorded (see Figure 4 (b)). The first point to be noted from these results is the higher signal to noise ratio of the data in comparison to those shown in Figures 3 (b) and (c) in spite of the significantly lower acquisition times (10 minutes/point for Figure 3 versus 1 minute/point for Figure 4). The reason for this is the higher efficiency of the single ion detection used in this method in comparison to the electron-ion-ion coincidence technique employed for the spectra in Figures 3 (b) and (c). However, the advantage of the higher collection efficiency is offset by the lack of ion momentum matching in the single ion detection. In this experiment the discrimination of the atomic and dimer signals is achieved on the basis of the kinetic energy of the detected ions. The faster ions (KE > 0.75 eV) can only arise from Coulomb explosion of the dimer ions due to processes which take place subsequent to the initial resonant absorption. The efficacy of the technique is confirmed by the comparison of the spectra shown in Figure 4 (a) with the equivalent coincidence data shown in Figure 3 (c). In particular, examination of the inset in Figure 4 (a) confirms the positive energy shift of the $2p_{1/2}^{-1}4s$ peak and the
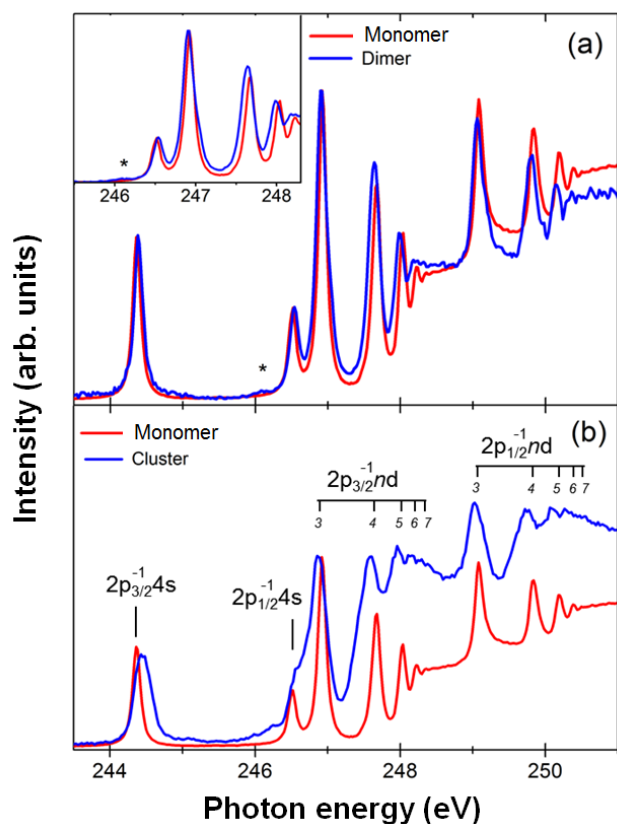
Fig. 4: (a) The ion yield spectra recorded using the experimental set-up in Figure 1 (b) for pure Argon expansion conditions where only Argon monomers and dimers are present in the beam. Blue line: the yield of low kinetic energy ions; red lines: the yield of ions with KE > ~0.75 eV. The inset shows a higher resolution spectrum in the region of the $2p_{1/2}^{-1}4s$, $2p_{3/2}^{-1}3d$, $2p_{3/2}^{-1}4d$ and $2p_{3/2}^{-1}5d$ resonances. (b) The same spectrum with beam expansion conditions such that there is a significant content of small clusters in the beam.

negative shifts of the $2p_{3/2}^{-1}3d$, $2p_{3/2}^{-1}4d$ and $2p_{3/2}^{-1}5d$ resonances of the Ar_2 dimer spectra in comparison to the monomer spectrum. In addition, it is apparent from Figure 4 (a) that the negative energy shift of the $2p_{3/2}^{-1}nd$ increases with increasing n. Further information extracted from Figure 4 (a) includes the negative shifts of the $2p_{1/2}^{-1}nd$ resonances not recorded in the coincidence data shown in Figure 3 and the fact that the relative intensities of the peaks in the Ar_2 spectrum do not significantly change with respect to those in the atomic Ar spectrum. This latter point suggests that the anomalously large intensity of the $2p_{3/2}^{-1}4s$ peak in Figure 3 (c) may be due to a problem of normalisation caused by the composite nature of this spectrum recorded in a number of data acquisition runs. As a final point the increased signal to noise ratio of the KE filtered spectra allow the clear identification of the $2p_{3/2}^{-1}4p$ resonance in the dimer spectrum (marked by an asterisk in the inset of Figure 4 (a)) which was not observed in

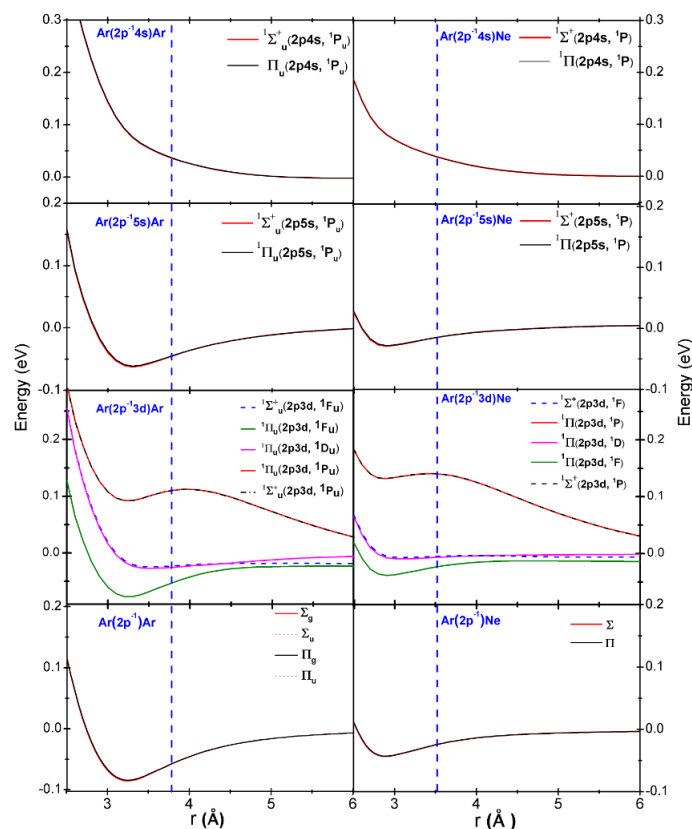the coincidence data. This state is dipole forbidden but becomes allowed due to the lower symmetry of the dimer.

Fig. 5: Computed potential energy curves of the lowest core-excited and core-ionized states of Ar_2 and ArNe which are dipole allowed at the dimer equilibrium distances. They correlate with the $Ar(2p^{-1}4s)$, $Ar(2p^{-1}5s)$, $Ar(2p^{-1}3d)$, $Ar^+(2p^{-1})$ excited states and a ground state neighbor at asymptotic interatomic distances. All computations were non-relativistic. The zero energy in the case of the $Ar(2p^{-1}5s)$, $Ar(2p^{-1}3d)$ PECs was chosen to correspond to the computed asymptotic energy of the dipole-allowed $Ar(2p^{-1}3d\ ^1P)Ar$ and $Ar(2p^{-1}3d\ ^1P)Ne$ states. The transition moments as a function of the internuclear distance for each of these states is shown in the supplementary information.

To understand the energy shifts of the dimer spectra in a quantitative manner the $2p^{-1}nl$ core-hole potential energy curves (PECs) of the Ar_2 and ArNe dimers were calculated. These PECs are presented in Figure 5. Visual inspection provides an immediate qualitative explanation for many of the experimental observations described above. The positive energy shifts of the $2p_{3/2}^{-1}4s$ and $2p_{1/2}^{-1}4s$ resonances in the dimer spectra is due to the repulsive nature of the $Ar(2p^{-1}4s)Ar$ and $Ar(2p^{-1}4s)Ne$ PECs. At the ground state equilibrium separation of the Ar_2 and ArNe dimers (3.80 and 3.52 Å) the potential energies of the $Ar(2p^{-1}4s)Ar$ and $Ar(2p^{-1}4s)Ne$ states are 34 meV and 38 meV higher than the respective asymptotic values. This clearly explains the positive shifts of the corresponding peaks in the dimer spectra. Another

interesting point to note is that the PECs of the Σ and Π symmetries (due to the orientation of the $2p^{-1}$ core-hole with respect to the internuclear axis) are almost identical. Therefore, it is clear that the $2p^{-1}$ core-hole orientation has a negligible effect on the binding energy as the 2p orbital is very compact and is essentially seen as an isotropic charge by the neighbouring atom. This observation is true for all PECs presented as can be confirmed from the comparison of the Σ and Π states also in the cases of the $Ar(2p^{-1}5s)$ and $Ar^+(2p^{-1})$ core-hole states and therefore we conclude that all symmetry effects are due to the excited Rydberg electron.

Visual inspection supports the same conclusion for $2p^{-1}3d$ states, where the orientation of the 3d orbital along the intermolecular axis determines its attractive or repulsive character [for the simpler case of a p orbital, see Figure 7 of [17]]. Let us note that the potential energy curves associated to a given core-hole state are qualitatively similar for Ar_2 and ArNe (as highlighted by our choice of colors for the curves), and that the quantitative differences can be rationalised in terms of the overlap between the excited Rydberg electron and the electrons of the partner atom. Because of the predominant role of the Rydberg electron, these potential energy curves are also similar to those of the equivalent core (Z+1) approximation (available for KAr,[41] which indeed we have used in our previous work[27]). Of course the latter similarity is only qualitative, due to the different overall symmetry and multiplicity, as well as to the different extent of the Rydberg orbital in the equivalent core (Z+1) approximation case. Let us finally note that, both for the "exact" PECs and the equivalent core (Z+1) approximation, as soon as the Rydberg electron encompasses the whole dimer, which is then seen as a single ionic core, the shape of all potential energy curves converges to that of the respective dimer ion.

In contrast to the $Ar(2p^{-1}4s)Rg$ PECs, the $Ar(2p^{-1}5s)Ar$ and $Ar(2p^{-1}5s)Ne$ core-hole states are weakly bound. The repulsive nature of the $Ar(2p^{-1}4s)Rg$ PECs versus the bound nature of the $Ar(2p^{-1}5s)Rg$ PECs can be understood in terms of the radial electron density of the respective excited electron. The radial density of the Ar 4s electron is peaked at ~ 3 Å which is comparable to the bond length in the dimer (see Figure 1 of the supplementary information) and hence there is a repulsion between the Rydberg electron and the neighbouring atom leading to the repulsive nature of the PEC. On the other hand, the radial electron density of the Ar 5s electron is peaked at ~ 6.5 Å which is larger than the internuclear distance and thus it is the attractive forces between the neighbour and the Ar^+ ion core of the excited state which dominate the potential leading to an attractive potential. This behaviour is similar to the effects observed for the PECs of $Ar^+(3p^{-2}$ $[^3P]4s)He$ and $Ar^+(3p^{-2}$ $[^3P]4s)He$ discussed in detail in[42].

The region containing the PECs of the $Ar(2p^{-1}3d)Ar$ and $Ar(2p^{-1}3d)Ne$ states has more complicated structure. The
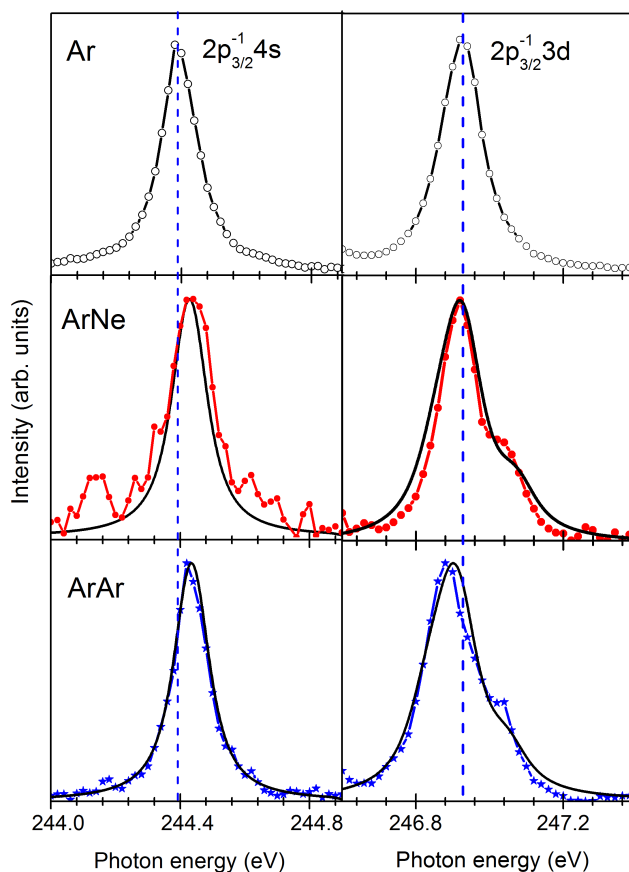

Fig. 6: Comparison of the simulated XAS spectra with the experimental data shown in Figure 3. The upper panels show the atomic XAS spectra in the $Ar(2p^{-1}4s)Ar$ and $Ar(2p^{-1}5s)Ar/Ar(2p^{-1}3d)Ar$ regions recorded using electron-Ar^+ coincidence technique. The middle panels show the comparison with simulated spectra (see text for details) for the ArNe dimer while the bottom panels show the comparison for Ar_2. The vertical dotted lines show the positions of the atomic resonances.

manifold of singlet $Ar(2p^{-1}3d)$ atomic states comprises the $Ar(2p^{-1}3d[^1P], [^1D], [^1F])$ states of which only the ^1P term, which is highest in energy, is optically allowed. In the dimer, each of the atomic terms splits into a number of molecular terms. As a result of the interaction between different molecular terms, five of them (three Π and two Σ^+ terms) acquire optical strength. As is evident from Fig. 5, the PECs of three of the molecular states, are weakly bound in the Franck-Condon region. This can account for the small negative shift of the peaks in the dimers' XAS spectra. This shift is however smaller for ArNe than for Ar_2. This fact can be explained with the smaller binding energy of these states at the respective equilibrium distances in ArNe as compared to Ar_2. The shoulder on the higher-energy side of the $Ar(2p^{-1}3d)Rg$ peaks can be understood as arising from the transition to the two highest $Ar(2p^{-1}3d[^1P])Rg$ states of the $Ar(2p^{-1}3d)$ manifold. These states exhibit quasibound regions at shorter internuclear distances. However, these regions are not accessible from the ground state of the dimer and do not contribute to the XAS spectra. The ground-state wave packet is therefore transferred onto the repulsive part of these curves, thus giving rise to the high energy shoulder on the "3d" resonance peak.

To test the quality of the PECs in a more quantitative manner we have performed Franck-Condon calculations on the transitions between the ground v=0 state and the PECs shown in Figure 5 in order to simulate the core-hole spectra. The results of these simulations for the $2p^{-1}4s$ and the $2p^{-1}5s/2p^{-1}3d$ resonances of both the Ar_2 and ArNe dimers are shown in Figure 6 where they are compared with the $2p_{3/2}^{-1}4s$ and $2p_{3/2}^{-1}5s/2p_{3/2}^{-1}3d$ resonances of the coincidence data from Figure 3. The details of these calculations are given in the computational methods section. For reference purposes the transition moments as a function of R for transitions to each of these states are given in Figure 2 of the supplementary information. The agreement between the calculated and experimental spectra is quite remarkable and demonstrates the quantitative accuracy of the PECs shown in Figure 5 as well as the calculation methods used to simulate the spectra.

Due to the complexity of the $2p_{3/2}^{-1}5s/2p_{3/2}^{-1}3d$ region of the spectra with transitions to 7 excited states contributing to the intensity we also show the contributions of the transitions to each of these states to the overall spectrum in Figure 7. Another point to consider is the possibility of symmetry effects due to the geometry of the experiment. Preferential detection of Σ or Π states is often used in soft X-ray absorption spectroscopy to gain information on the symmetry of the core-hole states being probed[43]. Here, in both experiments the electric field vector of the linearly polarized light is parallel to the TOF axes but while in the first method the Σ or Π states (absorbing dimers with the internuclear axis preferentially parallel and perpendicular to the TOF axis, respectively) are detected with the same efficiency, the second method is about 30% more efficient in detecting the Σ states with respect to the Π
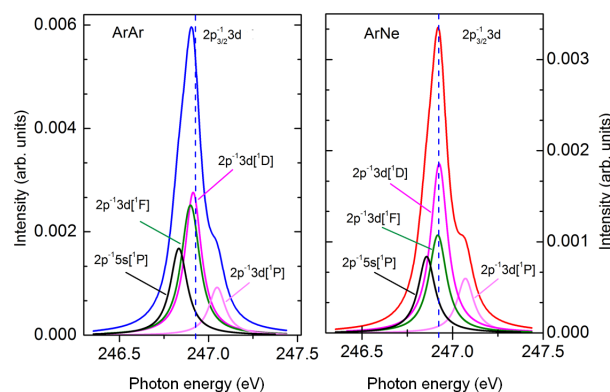

Fig. 7: Franck-Condon simulation of the $2p_{3/2}^{-1}5s/2p_{3/2}^{-1}3d$ resonance for the ArNe and Ar_2 dimers including contributions from different core-hole states. The natural line width of the 112 meV is convoluted with the FC calculations. The dotted lines show the position of the atomic resonance.

states. Nonetheless, careful inspection of Figures 5 and 7 show that the only unpaired state is the $^1\Pi$ $(2p^{-1}3d[^1F])$ state which does not significantly contribute to the shift or broadening of the $2p_{3/2}^{-1}3d$ in Ar_2 or ArNe. Therefore, we conclude that the shape of the $2p_{3/2}^{-1}5s/2p_{3/2}^{-1}3d$ resonance lines in the dimers is not sensitive to the symmetry effects due to the geometry of the measurements.

The higher $2p^{-1}nd$ states can be considered to be intermediate cases between the $2p^{-1}3d$ states described above and the $Ar^+(2p^{-1})Ar$ and $Ar^+(2p^{-1})Ne$ core-hole ion states. Both ion states are weakly bound with the $Ar^+(2p^{-1})Ar$ PECs showing a minimum of 85 meV at 3.2 Å and the $Ar^+(2p^{-1})Ne$ PECs with a minimum of 43 meV at 2.9 Å with respect to the atomic value. To obtain a deeper insight into the shifts of the higher $2p^{-1}nd$ resonances in the dimer XAS spectra with respect to the atom we have performed FC calculations on the transitions between the v=0 vibrational level of the ground state of the Ar_2 and ArNe dimers and the corresponding $2p^{-1}$ core-hole ion states (the PECs of which are shown in the lower panels of Figure 5) using LEVEL[44]. The results of these calculations are shown in Figure 8 where it can be seen that the negative shifts of the core-hole transitions with respect to the Ar atom are 40 meV and ~20 meV in the cases of the Ar_2 and ArNe dimers, respectively. These shifts are consistent with the experimentally observed shifts of the high $2p^{-1}nd$ (n = 4-6) transitions which can be seen in Figures 3 and 4. Furthermore, the smaller extent of the experimentally observed shifts of these resonances in the ArNe dimer (see Figures 3 (b)) in comparison to the Ar_2 dimer is consistent with these calculations.

In light of the above discussions we can now return to briefly discuss the small Ar cluster spectrum shown in Figure 4 (d). Here, as noted above, it is possible to see larger shifts of the $2p^{-1}4s$ peak (+85 meV) and the $2p^{-1}5s/2p^{-1}3d$ (-65 meV) as well as significantly more broadening with respect to the dimer spectra. For the Ar $2p^{-1}4s$ peak we know that the dimer shift is 38 meV
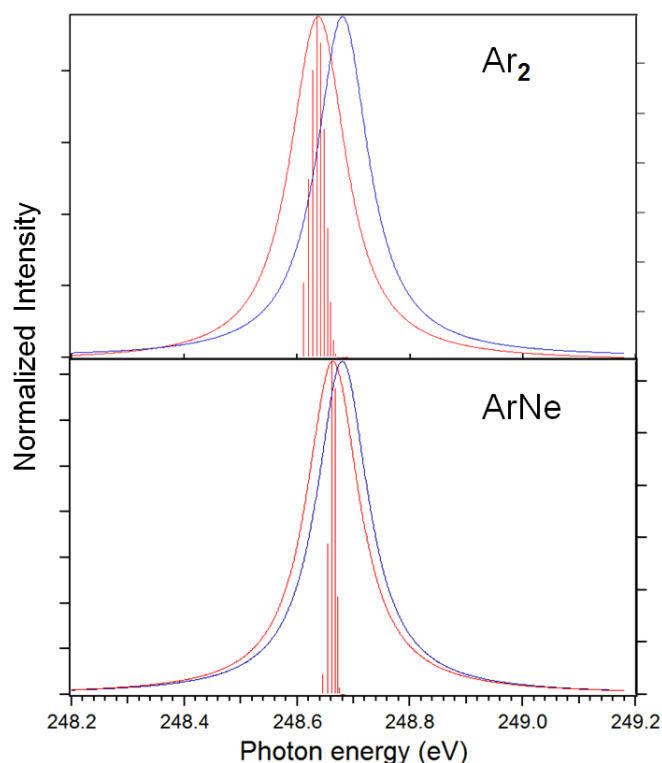
Fig. 8: Franck-Condon calculations for the excitation process from the v=0 ground state of ArNe and Ar_2 and the corresponding $2p^{-1}$ ion-core hole states referenced to the ionization of the $Ar^+(2p^{-1}_{3/2})$ level at 248.68 eV[45].

while the trimer shift is predicted from $2p^{-1}4s$ modelling in Ar clusters to be approximately 100 meV (see Fig. 1 of ref[8]). The shift observed suggests that the most probable cluster is the Ar_3 trimer however considering the significant broadening to higher energies it is clear that the spectrum contains contributions from at least Ar_n, n = 2-5. This is consistent with the measured shift of $\sim$ 230 meV (extracted from Fig. 1 of ref[7]) for a cluster distribution of average size n=5. It is clear that the spectral region in the vicinity of the $2p^{-1}5s/2p^{-1}3d$ is much more complicated due to the large broadening and shifts which result in merging of the $2p^{-1}5s/2p^{-1}3d$ with the nearby $2p^{-1}_{1/2}4s$ peak. Therefore, this region of the spectrum is not suitable for size/structure determination of the clusters.

5   Conclusions

The XAS spectra of rare gas dimers and small clusters have been investigated by using synchrotron light to excite core-hole states of the Ar containing dimers and small clusters in the $L_{2,3}$-edge region. Two experimental methods have been used, the first of which involves the detection of an electron and two ions in coincidence as a method to select events due to core-hole excitation of the Ar_2 and ArNe dimers from the events due to monomers in the

same beam. The second method, on the other hand, is based on the discrimination of the kinetic energy of the ions formed due to processes involving Coulomb explosions of the multiply charged dimers and clusters formed following core-hole excitation and the low KE ions formed in the monomer. Both methods allow us to observe very small shifts of the core-hole resonances (well below the natural width of the resonances) of the dimers and small clusters in comparison to the atomic spectrum. These shifts and peak shape changes are directly related to the PECs of the core hole excited states in the Ar_2 and ArNe dimers. The PECs have been calculated by the ADC(2) extended *ab initio* method and the XAS spectra have been simulated by performing FC calculations for transitions between the ground state of the corresponding dimer and these core-hole PECs. The simulated spectra are in remarkable agreement with the experimental spectra of the Ar_2 and ArNe dimers showing the quantitative accuracy of the PECs and the FC calculations. This quantitative understanding of the dimer spectra indicates that the small positive shifts of the $Ar(2p^{-1}4s)$ in the dimers is related to the repulsion between the excited Rydberg electron and the neighbouring atom. This explains why additive theories based on the repulsion with nearest neighbours work so well when modelling the shifts in large Ar containing clusters and thus why this core hole resonance is useful in structure determination of large clusters. In contrast, the shifts in the region of the spectrum containing the $Ar(2p^{-1}5s)$ and $2p^{-1}3d$ resonances are much more complicated due to contributions of both bound and repulsive core-hole states and therefore this region of the spectrum is not a good candidate for structure determination.

Notes and references

1 H. Wende, *Reports on Progress in Physics*, 2004, **67**, 2105.

2 C. Miron and P. Morin, in *High resolution Inner shell Photoionization, Photoelectron and Coincidence Spectroscopy*, John Wiley & Sons, Ltd, 2011.

3 O. Björneholm, G. Öhrwall and M. Tchaplyguine, *Nucl. Instrum. Methods Phys. Res., Sect. A*, 2009, **601**, 161 – 181.

4 G. Hahner, *Chem. Soc. Rev.*, 2006, **35**, 1244–1255.

5 E. Rühl, C. Heinzel, A. P. Hitchcock and H. Baumgärtel, *J. Chem. Phys.*, 1993, **98**, 2653–2663.

6 A. Pavlychev, E. Semenova, A. Hitchcock and E. Rühl, *Physica B: Condensed Matter*, 1995, **208**, 187 – 189.

7 O. Björneholm, F. Federmann, F. Fössing and T. Möller, *Phys. Rev. Lett.*, 1995, **74**, 3017–3020.

8 J. P. Gauyacq, *Phys. Rev. B*, 2005, **71**, 115433.

9 O. Björneholm, *Surf. Rev. Lett.*, 2002, **09**, 3–12.

10 M. Tchaplyguine, R. Feifel, R. Marinho, M. Gisselbrecht, S. Sorensen, A. N. de Brito, N. Mårtensson, S. Svensson and O. Björneholm, *Chem. Phys.*, 2003, **289**, 3 – 13.

11 T. Hatsui, M. Nagasono and N. Kosugi, *J. Electr. Spectr. Relat. Phenom.*, 2004, **137**, 435.

12 A. Lindblad, T. Rander, I. Bradeanu, G. Öhrwall, O. Björneholm, M. Mucke, V. Ulrich, T. Lischke and U. Hergenhahn, *Phys. Rev. B*, 2011, **83**, 125414.

13 J. P. Gauyacq and A. G. Borisov, *Phys. Rev. B*, 2004, **69**, 235408.

14 J. Gauyacq and A. Kazansky, *Chem. Phys.*, 2006, **327**, 300 – 310.

15 D. Marinica, C. Ramseyer, A. Borisov, D. Teillet-Billy and J. Gauyacq, *Surface Science*, 2003, **540**, 457 – 473.

16 L. Kleinman and D. M. Bylander, *Phys. Rev. Lett.*, 1982, **48**, 1425–1428.

17 W. E. Baylis, *J. Chem. Phys.*, 1969, **51**, 2665–2679.

18 J. Pascale and J. Vandeplanque, *J. Chem. Phys.*, 1974, **60**, 2278–2289.

19 J. F. Dawson and L. C. Balling, *J. Chem. Phys.*, 1979, **71**, 836–842.

20 S. Ossicini and F. Forstmann, *J. Chem. Phys.*, 1981, **75**, 2076–2079.

21 W. L. Jolly and D. N. Hendrickson, *J. Am. Chem. Soc.*, 1970, **92**, 1863–1871.

22 M. N. R. Wohlfarth and L. S. Cederbaum, *J. Chem. Phys.*, 2002, **116**, 8723–8730.

23 K. Gokhberg, P. Kolorenč, A. I. Kuleff and L. S. Cederbaum, *Nature*, 2014, **505**, 661–663.

24 T. Miteva, Y.-C. Chiang, P. Kolorenč, A. I. Kuleff, K. Gokhberg and L. S. Cederbaum, *J. Chem. Phys.*, 2014, **141**, 064307.

25 T. Miteva, Y.-C. Chiang, P. Kolorenč, A. I. Kuleff, L. S. Cederbaum and K. Gokhberg, *J. Chem. Phys.*, 2014, **141**, 164303.

26 M. Kimura, H. Fukuzawa, T. Tachibana, Y. Ito, S. Mondal, M. Okunishi, M. Schöffler, J. Williams, Y. Jiang, Y. Tamenori, N. Saito and K. Ueda, *J. Phys. Chem. Lett.*, 2013, **4**, 1838–1842.

27 P. O'Keeffe, E. Ripani, P. Bolognesi, M. Coreno, M. Devetta, C. Callegari, M. Di Fraia, K. C. Prince, R. Richter, M. Alagia, A. Kivimäki and L. Avaldi, *J. Phys. Chem. Lett.*, 2013, **4**, 1797–1801.

28 F. Trinter, M. S. Schöffler, H.-K. Kim, F. Sturm, K. Cole, N. Neumann, A. Vredenborg, J. Williams, I. Bocharova, R. Guillemin, M. Simon, A. Belkacem, A. L. Landers, T. Weber, H. Schmidt-Böcking, R. Dörner and T. Jahnke, *Nature*, 2014, **505**, 664–666.

29 S. M. Cybulski and R. R. Toczylowski, *J. Chem. Phys.*, 1999, **111**, 10520–10528.

30 J. Schirmer, L. S. Cederbaum and O. Walter, *Phys. Rev. A*, 1983, **28**, 1237–1259.

31 A. B. Trofimov and J. Schirmer, *J. Phys. B: At., Mol. Opt. Phys.*, 1995, **28**, 2299.

32 L. S. Cederbaum, W. Domcke, J. Schirmer and W. von Niessen, *Phys. Scr.*, 1980, **21**, 481.

33 D. E. Woon and T. H. Dunning, *J. Chem. Phys.*, 1993, **98**, 1358–1371.

34 G. Karlström, R. Lindh, P.-Å. Malmqvist, B. O. Roos, U. Ryde, V. Veryazov, P.-O. Widmark, M. Cossi, B. Schimmelpfennig, P. Neogrady and L. Seijo, *Comput. Mater. Sci.*, 2003, **28**, 222 – 239.

35 K. Kaufmann, W. Baumeister and M. Jungen, *J. Phys. B: At., Mol. Opt. Phys.*, 1989, **22**, 2223.

36 T. H. Dunning, *J. Chem. Phys.*, 1989, **90**, 1007–1023.

37 D. T. Colbert and W. H. Miller, *J. Chem. Phys.*, 1992, **96**, 1982–1991.

38 M. Kato, Y. Morishita, M. Oura, H. Yamaoka, Y. Tamenori, K. Okada, T. Matsudo, T. Gejo, I. Suzuki and N. Saito, *J. Electr. Spectr. Relat. Phenom.*, 2007, **160**, 39 – 48.

39 R. R. Blyth, R. Delaunay, M. Zitnik, J. Krempasky, R. Krempaska, J. Slezak, K. C. Prince, R. Richter, M. Vondracek, R. Camilloni, L. Avaldi, M. Coreno, G. Stefani, C. Furlani, M. de Simone, S. Stranges and M.-Y. Adam, *J. Elec. Spectrosc. Relat. Phenom.*, 1999, **101-103**, 959–964.

40 E. Keshavarz, H. Farrokhpour, H. Sabzyan, Z. Noorisafa, A. Kivimäki and R. Richter, *Phys. Rev. A*, 2014, **89**, 053409.

41 M. B. El-Hadj-Rhouma, H. Berriche, Z. B. Lakhdar and F. Spiegelman, *J. Chem. Phys.*, 2002, **116**, 1839–1849.

42 T. Miteva, S. Klaiman, E. V. Gromov and K. Gokhberg, *J. Chem. Phys.*, 2014, **140**, 204320.

43 J. Adachi, N. Kosugi and A. Yagishita, *J. Phys. B: At., Mol. Opt. Phys.*, 2005, **38**, R127.

44 R. J. Le Roy, Level 8.0: A Computer Program for Solving the Radial Schrödinger Equation for Bound and Quasibound Levels, University of Waterloo Chemical Physics Research Report CP-663 (2007); see http://leroy.uwaterloo.ca/programs/.

45 G. C. King, M. Tronc, F. H. Read and R. C. Bradford, *J. Phys. B: At., Mol. Opt. Phys.*, 1977, **10**, 2479.